18th AIAA/CEAS Aeroacoustics Conference (33rd AIAA Aeroacoustics Conference)
04 - 06 June 2012, Colorado Springs, CO
AIAA 2012-2149

Prediction of subsonic jet noise relying on a sweeping based turbulence generation process

Anthony Lafitte*

Liebherr-Aerospace, 31016 Toulouse, France

Thomas Le Garrec†

Onera - The French Aerospace Lab F-92322 Châtillon, France

Christophe Bailly‡

Ecole Centrale Lyon, 69134 Ecully, France

Estelle Laurendeau§

Liebherr-Aerospace, 31016 Toulouse, France

Jet pumps, which are considered in the framework of this study as simple jets confined in ducts, could be a significant ally in the mission of the aeroacoustic community to make the aircraft more environmentally friendly. Despite the significant gains that it could bring for various functions of the systems of the engines, such devices could contribute directly to ramp noise. Therefore, a predictive code of the noise radiated by these configurations could be a useful tool to propose noise reduction solutions. A numerical tool, designed for acoustic prediction of confined jets, is presented in this paper. The proposed method is adapted to industrial requirements since it is easily implementable and applicable to any 3D configuration. The acoustic propagation is obtained by computing the response of the linearized Euler equations, enforced by a non-linear source term calculated with a stochastic velocity field synthetized from the sweeping based turbulence generation process proposed by Lafitte *et al.* [AIAA 2011-2088]. The chosen formulation is validated by computing test cases including simple dipole and quadrupole distributions. The predictive tool is then applied to a cold free jet configuration at Mach number M=0.72. Preliminary computations show that the forcing of the linearized Euler equations by a stochastic source term appears to be a complex operation since far-field acoustic spectra levels are overestimated. An accurate calibration method of the acoustic source term is therefore introduced in the present work.

I. Introduction

The cabin air conditioning is of paramount importance for the passengers and crew comfort aboard an aircraft. Working on the optimization of the systems ensuring the bleed, cooling, drying and transportation of the conditioned air to the cabins of the engines, Liebherr Aerospace (LTS) plans to improve its packs efficiency to make them more environmentally friendly. To do that, few modifications have therefore been tested. One of these concepts is to integrate jet pumps which could offer significant gains over the current technologies for various functions of the systems. Assuming that these devices could contribute directly to ramp noise, the use of a numerical tool to predict acoustics of jet pumps could help to propose, if the need arises, appropriate noise reduction solutions.
A numerical tool designed to predict far-field acoustics is presented in this paper. The chosen methodology, inspired by the literature,[1–3] fits Liebherr's industrial needs since it presents the advantages of being easily implementable, applicable to any 3D configurations and relatively inexpensive in CPU time. Using

*PhD Student, Research and Expertise Department, anthony.lafitte@liebherr.com
†Research Engineer, Computational Fluid Dynamics and Aeroacoustics Department, thomas.le_garrec@onera.fr
‡Professor, Senior Member AIAA, christophe.bailly@ec-lyon.fr
§Research Engineer, Research and Expertise Department,estelle.laurendeau@liebherr.com

the Onera's Euler solver *sAbrinA_v0*, the far-field acoustic radiation is obtained by solving the linearized Euler equations (LEE) which are explicitely enforced by a preliminary built non-linear source vector. The unsteady velocity field which is needed to compute the source terms is synthetized directly from the sweeping based turbulence generation process proposed by Lafitte *et al.*[4]

The formulation of the linearized Euler equations used in the present work is presented in section II. The abilities of the numerical solver to preserve the multipolar features of a given source and to predict acoustic refraction due to the presence of a sheared mean flow have been checked by computing test cases, including the forcing of the linearized Euler equations by dipole and quadrupole distributions. The sweeping based turbulence generation process allowing the calculation of the injected source terms is recalled in the section III. In section IV, the predictive tool is applied to a free subsonic jet configuration, Onera's Φ_{80} at M=0.72, since the confined geometry is too complicated to be investigated at first.

II. Linearized Euler equations with source terms

A. Description of Euler solver *sAbrinA_v0*

The CAA calculations were conducted with ONERA's *sAbrinA_v0* solver.[5,6] *sAbrinA_v0* is a structured grid, time-accurate CAA code that solves either the full or the linear Euler equations, in a conservative and perturbed form (with a splitting of the complete variables into a "frozen" mean flow and a "fluctuating" perturbation). The solver employs high-order, finite-difference operators, involving 6th-order spatial derivatives and 10th-order filters, as well as a 3rd-order, multi-stage, Runge-Kutta time-marching scheme. The code deals with multi-block structured grids with one-to-one interfaces, and is fully parallelized using the Message Passing Interface (MPI) standard. Finally, the solver includes the usual boundary conditions (reflection by solid walls, non-reflecting / free-field radiation,[5–7] etc.), as well some unique to specific applications (such as the surface coupling technique[5,6]). Finally, it can be pointed out that such CAA solver is parallelized (in a MPI - Message Passing Interface sense), which offered to run the present calculations in parallel. More detailed information about the *sAbrinA_v0* solver and its underlying methodology can be found in Ref. [5,6]. One can remind that the free-field radiation through peripheral boundaries is mimicked with the help of an as simple as efficient technique; originally proposed in Ref. [5,6] and accurately assessed / validated in Ref. [7], such technique is based on a progressive decreasing of the spatial derivatives / filters accuracy order (to be obtained via a reduction of the schemes stencil half-width). Coupled with a rapid grid stretching (over 6 peripheral rows of ghost points), this trick allows the perturbations to leave properly the calculation domain - that is to say without generating significant numerical reflections at the frontiers.

B. Formulation of the linearized Euler equations

The set of equations implemented in the code *sAbrinA_v0* is in conservative form and perturbed variables. In the present work, only the linearized form of the equations, defined in Eq. (1), is used; the left hand side of the system being explicitely forced by a source vector $\mathbf{S}$ located at the right hand side. The density ρ', the velocity $\mathbf{u}' = (u'_1, u'_2, u'_3)$ and the pressure p' represent small pertubations superimposed on a mean flow of density $\overline{\rho}$, velocity $\overline{\mathbf{u}}$ and pressure $\overline{p}$. Considering that the mean flow is solution of the Euler equations, the linearized equations may be written as

$$\frac{\partial \mathbf{U}}{\partial t} + \frac{\partial \mathbf{F}}{\partial x} + \frac{\partial \mathbf{G}}{\partial y} + \frac{\partial \mathbf{H}}{\partial z} = \mathbf{S} \tag{1}$$

where $\mathbf{U}$ designates the unknown vector:

$$\mathbf{U} = \begin{pmatrix} \rho' \\ \rho' \overline{u}_1 + \overline{\rho} u'_1 \\ \rho' \overline{u}_2 + \overline{\rho} u'_2 \\ \rho' \overline{u}_3 + \overline{\rho} u'_3 \\ \overline{\rho}\ \overline{u}_k u'_k + \dfrac{1}{2}\rho' \overline{u}_k^2 + \dfrac{1}{\gamma - 1} p' \end{pmatrix} \tag{2}$$

where $\mathbf{F}$, $\mathbf{G}$ and $\mathbf{H}$ refer respectively to the flux vectors according to directions x, y and z. The flux vectors are given by the following definitions:

$$\mathbf{F} = \begin{pmatrix} \rho' \overline{u}_1 + \overline{\rho} u'_1 \\ 2\overline{\rho}\ \overline{u}_1 u'_1 + p' + \rho' \overline{u}_1^2 \\ \rho' \overline{u}_1\ \overline{u}_2 + \overline{\rho} u'_1 \overline{u}_2 + \overline{\rho}\ \overline{u}_1 u'_2 \\ \rho' \overline{u}_1\ \overline{u}_3 + \overline{\rho} u'_1 \overline{u}_3 + \overline{\rho}\ \overline{u}_1 u'_3 \\ u'_1 \left(\frac{1}{2}\overline{\rho}\ \overline{u}_k^2 + \frac{\gamma}{\gamma - 1}\overline{p} \right) + \overline{u}_1 \left(\overline{\rho}\ \overline{u}_k u'_k + \frac{1}{2}\rho' \overline{u}_k^2 + \frac{\gamma}{\gamma - 1} p' \right) \end{pmatrix}$$

$$\mathbf{G} = \begin{pmatrix} \rho' \overline{u}_2 + \overline{\rho} u'_2 \\ \rho' \overline{u}_2\ \overline{u}_1 + \overline{\rho} u'_2 \overline{u}_1 + \overline{\rho}\ \overline{u}_2 u'_1 \\ 2\overline{\rho}\ \overline{u}_2 u'_2 + p' + \rho' \overline{u}_2^2 \\ \rho' \overline{u}_2\ \overline{u}_3 + \overline{\rho} u'_2 \overline{u}_3 + \overline{\rho}\ \overline{u}_2 u'_3 \\ u'_2 \left(\frac{1}{2}\overline{\rho}\ \overline{u}_k^2 + \frac{\gamma}{\gamma - 1}\overline{p} \right) + \overline{u}_2 \left(\overline{\rho}\ \overline{u}_k u'_k + \frac{1}{2}\rho' \overline{u}_k^2 + \frac{\gamma}{\gamma - 1} p' \right) \end{pmatrix}$$

$$\mathbf{H} = \begin{pmatrix} \rho' \overline{u}_3 + \overline{\rho} u'_3 \\ \rho' \overline{u}_2\ \overline{u}_1 + \overline{\rho} u'_2 \overline{u}_1 + \overline{\rho}\ \overline{u}_2 u'_1 \\ 2\overline{\rho}\ \overline{u}_2 u'_2 + p' + \rho' \overline{u}_2^2 \\ \rho' \overline{u}_2\ \overline{u}_3 + \overline{\rho} u'_2 \overline{u}_3 + \overline{\rho}\ \overline{u}_2 u'_3 \\ u'_3 \left(\frac{1}{2}\overline{\rho}\ \overline{u}_k^2 + \frac{\gamma}{\gamma - 1}\overline{p} \right) + \overline{u}_3 \left(\overline{\rho}\ \overline{u}_k u'_k + \frac{1}{2}\rho' \overline{u}_k^2 + \frac{\gamma}{\gamma - 1} p' \right) \end{pmatrix}$$

In the system of equations (1), if the source vector $\mathbf{S}$ is known, the left hand side of the system is a linear propagator responding to that source. In the framework of this study, the following source vector is enforced in the LEE:

$$\mathbf{S} = \beta \begin{pmatrix} 0 \\ -\dfrac{\partial}{\partial x_j} \overline{\rho} u'_1 u'_j \\ -\dfrac{\partial}{\partial x_j} \overline{\rho} u'_2 u'_j \\ -\dfrac{\partial}{\partial x_j} \overline{\rho} u'_3 u'_j \\ 0 \end{pmatrix} \tag{3}$$

with β a calibration factor. One can remark that the source vector $\mathbf{S}$ formed with $\beta = 1$ is equivalent with the source term used by Bogey & Bailly.[8] In the present work, the mean flow variables are provided by a steady RANS computation and the source vector is computed directly from an unsteady velocity field generated from the stochastic process presented in section III.

C. Validation of the present formulation

The implementation of the source vector in the linearized Euler equations is investigated in this subsection. Three test cases are performed in order to check the validity of the present formulation. The wave propagator,

which is at the left hand side of the system of equations (1), needs to be able to preserve the multipolar features of a given source. The acoustic radiation emitted by dipolar and quadrupolar sources is therefore investigated. As well, the chosen formulation has to deal correctly with the refraction effects due to the presence of an inhomogeneous mean flow. This is checked by studying the acoustic radiation of an inflow quadrupole distribution. The present work results are compared to analytical solutions and to numerical data obtained by Bailly & Juvé.[3] Numerical simulations are computed on a $2D$ regular cartesian grid constituted of 400×400 points so that $-200 < x, y < 200$ m. The spatial resolution is set to $\Delta x = \Delta y = 1$ m. A time step of $\Delta t = \Delta x / c_0$ is imposed in order to work with $CFL = 1$. The idea is to enforce the linearized Euler equations by a given source distribution at the center of the grid to check the ability of the numerical solver to reconstrusct properly the acoustic radiation in the far-field.

1. Dipole distribution

A $2D$ dipole distribution F_i is first introduced :

$$\begin{cases} F_1 = B \cos\left(\dfrac{\pi}{10} x\right) e^{-\alpha y^2} \sin(\omega t) \\ F_2 = 0 \\ (x, y) \in [-5; 5] \times \Re \end{cases} \tag{4}$$

The amplitude B of the source is set to the value 0.01, the angular frequency to $\omega \Delta t = 2\pi/60$ and $\alpha = (\ln 2)/5$. The dipole distribution F_i is used to enforce the linearized Euler equations. One can therefore note that

$$\mathbf{S} = \begin{pmatrix} 0 \\ F_1 \\ F_2 \\ 0 \end{pmatrix} \tag{5}$$

The exact solution of this configuration is given by the convolution product $\rho' = -F_1 \otimes \partial G / \partial x$, where the Green's function G is written

$$G(\mathbf{x}, t) = \frac{\partial}{\partial x} \frac{i}{4 c_0^2} H_0^{(1)}\left((\omega / c_0) r\right) e^{-i\omega t} \tag{6}$$

where $\mathbf{x}$ is defined by the coordinates (x,y) and $r = \sqrt{x^2 + y^2}$. $H_0^{(1)}$ designates the zeroth-order Hankel function of the first kind. Fig. 1 shows pressure isocontours at the physical time $t = 640 \Delta t$ in the computational domain. The dipolar structure of the acoustic radiation is recovered by the numerical solver.

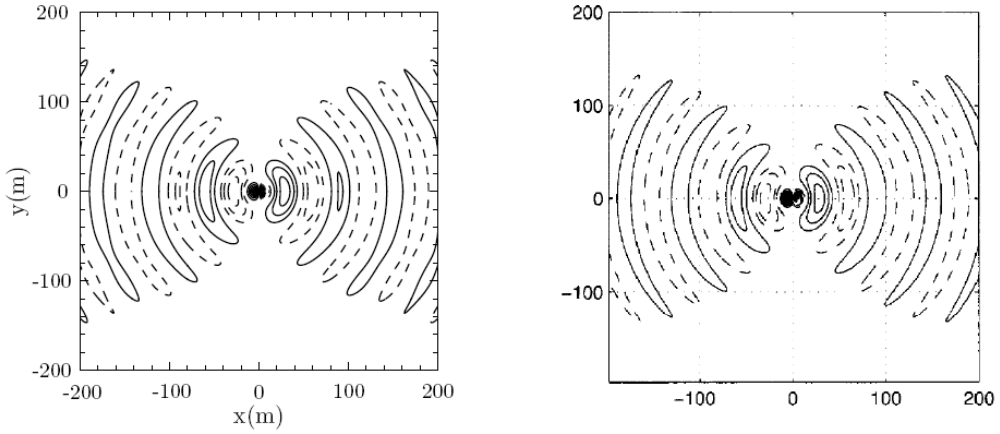

a) *b)*

Figure 1. Dipolar distribution $S_i = F_i$, pressure isocontours in the computation domain at time $t = 640\Delta t$ *a)* present work, *b)* obtained by Gréverie & Bailly[9] and Bailly & Juvé.[3] ━━ Positive values between 0.001 and 0.011 with a step size of 0.001, - - - Negative values.

The snapshot of the pressure field is identical to those obtained by Gréverie & Bailly[9] and Bailly & Juvé.[3] The fluctuating pressure along the axis $y = 0$ are plotted for two different time steps in the Fig. 2 and compared to the analytical solution. Both are in good agreement.

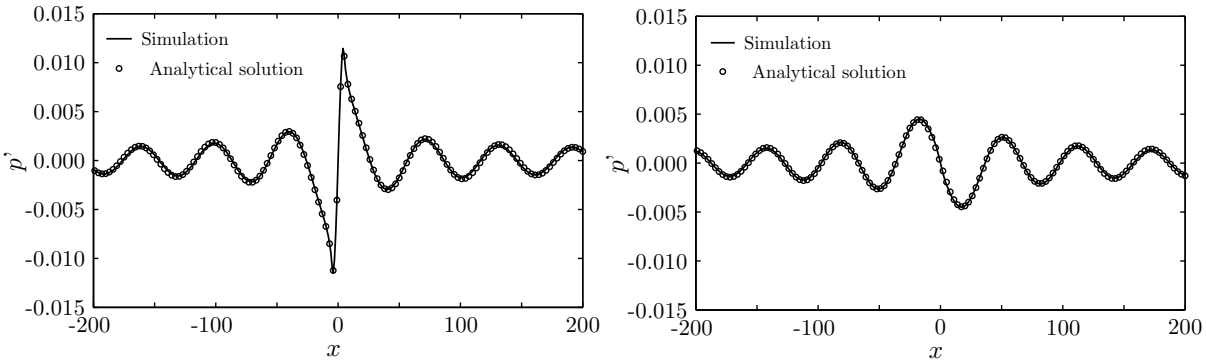

a) *b)*

Figure 2. Dipolar distribution $S_i = F_i$. Pressure profiles along the axis $y = 0$ at the time *a)* $t = 560\Delta t$, *b)* $t = 720\Delta t$.

2. Quadrupole distribution

A $2D$ quadrupole distribution T_{ij} is now studied. This distribution, expressed by the relation

$$T_{ij} = B\frac{20}{\pi}\begin{bmatrix} -\cos\left(\frac{\pi}{20}x\right)e^{-\alpha y^2} & 0 \\ 0 & \cos\left(\frac{\pi}{20}y\right)e^{-\alpha x^2} \end{bmatrix}\sin(\omega t) \tag{7}$$

is only defined on the interval $(x, y) \in [-10; 10] \times \Re$. The amplitude B of the source is set to the value 0.01, the angular frequency to $\omega\Delta t = 2\pi/60$ and $\alpha = (\ln 2)/5$. The forcing of the linearized Euler equations is achieved by imposing

$$\mathbf{S} = \begin{pmatrix} 0 \\ \frac{\partial}{\partial x_j}T_{1j} \\ \frac{\partial}{\partial x_j}T_{2j} \\ 0 \end{pmatrix} \tag{8}$$

The analytical solution of this test case is obtained by the following sum of convolution products:

$$\rho' = -\frac{\partial T_{11}}{\partial x} \otimes \frac{\partial G}{\partial x} - \frac{\partial T_{22}}{\partial y} \otimes \frac{\partial G}{\partial y}$$

where the Green's function is given by eq. (6). Fig. 3 shows the instantaneous pressure isocontours at the time $t = 640\Delta t$. The quadrupolar structure of the acoustic radiation, showed in Fig. 3 *a*), is correctly reconstructed and comparable to those obtained by Gréverie & Bailly[9] and Bailly & Juvé[3] which is depicted in Fig. 3 *b*).

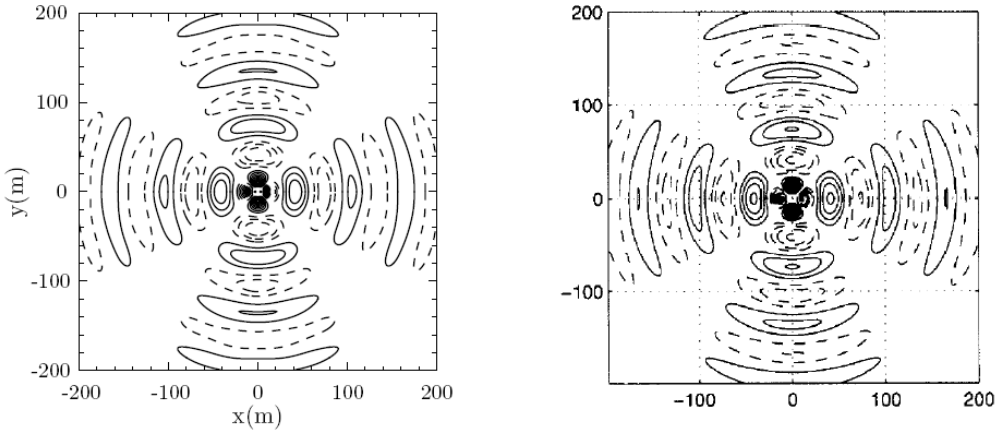

a) *b)*

Figure 3. Quadrupole distribution $S_i = \partial T_{ij}/\partial x_j$, pressure isocontours in the computational domain at time $t = 640\Delta t$ *a)* present work, *b)* obtained by Gréverie & Bailly[9] and Bailly & Juvé.[3] ━━ Positive values between 0.001 and 0.011 with a step size of 0.001, ▬ ▬ ▬ Negative values.

The evolution of the pressure fluctuations along the axis $y = 0$ for two different time steps are depicted in Fig. 4 and superimposed to the analytical solution. The curves obtained with the Euler solver perfectly match the analytical solution.

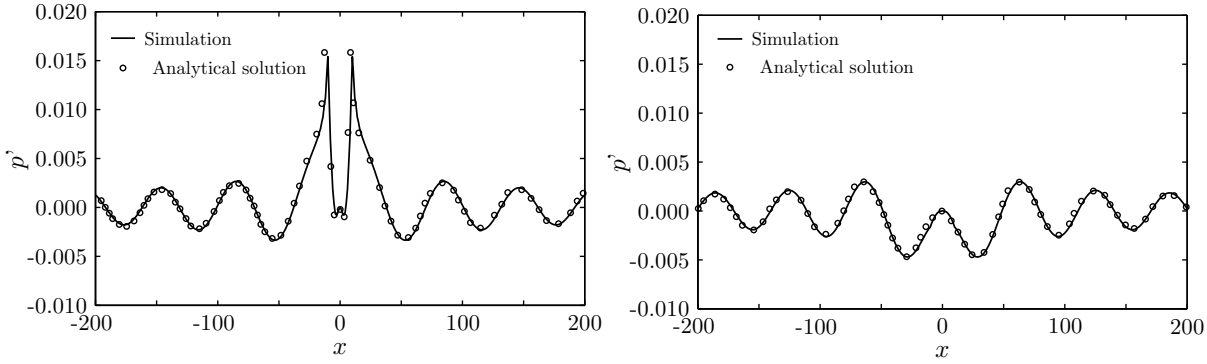

a) *b)*

Figure 4. Quadrupole distribution $S_i = \partial T_{ij}/\partial x_j$. Pressure profiles along the axis $y = 0$ at the time *a)* $t = 560\Delta t$, *b)* $t = 720\Delta t$.

3. Inflow quadrupole distribution

The objective of the third test case is to check that the numerical solver takes correctly into account the refraction effects due to the presence of a sheared mean flow. To do that, tha quadrupole distribution T_{ij} imposed in the subsection II.C.2 is placed on the axis of a fully developed two-dimensional jet at M= 0.5 modeled by a Bickley's profile given in its dimensionless form by

$$\frac{\overline{u}}{c_o} = \frac{0.5}{\cosh^2\left[(1+\sqrt{2})y/b\right]} \tag{9}$$

where the half-width b is equal to 20. The instantaneous pressure field in the computational domain is plotted in Fig. 5 for a given time $t = 640/(1+\mathrm{M})\Delta t$. The quadrupole nature of the acoustic radiation is preserved but the directivity is highly altered by the presence of the inhomogeneous mean flow.

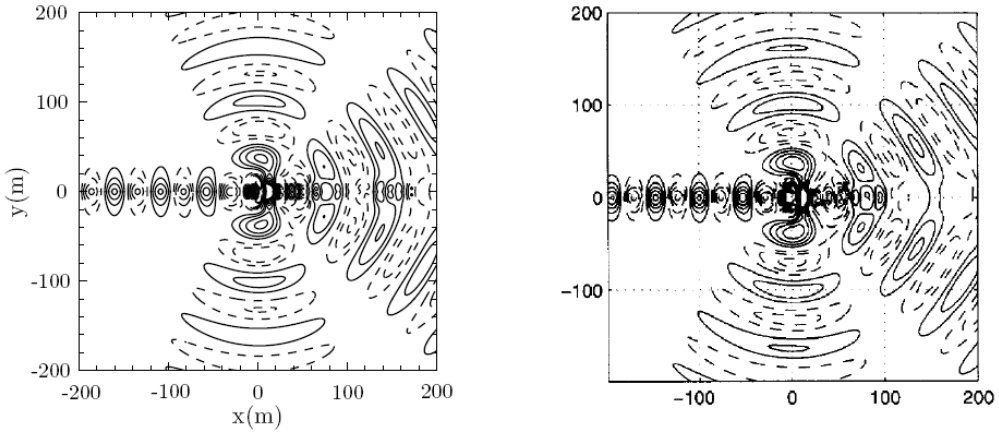

a) *b)*

Figure 5. Inflow quadrupole distribution $S_i = \partial T_{ij}/\partial x_j$. Instantaneous pressure field in the computational domain at the physical time $t = 640/(1+M)\Delta t$ *a)* present work, *b)* obtained by Gréverie & Bailly.[9] Axial Mach number is equal to M= 0.5. ━━ Positive values betwenn 0.001 and 0.011 with a step size of 0.001, - - - Negative values.

One can remark the creation of a shadow zone for small angles in the downstream direction and the focus of the acoustic waves on the axis of the jet in the upstream direction. Present results are in good agreement with those of Gréverie & Bailly[9] and Bailly & Juvé.[3]

The results of the three test cases show that the acoustic wave propagator is correctly reconstructed numerically from this set of linearized Euler equations: *i*) the wave propagator noticeably preserves the multipolar feature of a given source, *ii*) it correctly deals with the mean flow effects.

III. Turbulence generation process

In the present methodology, the acoustic propagation in the far-field outside the jet pump is obtained by solving the linearized Euler equations - the latter being explicitely enforced at each time step by an acoustic source vector that depends on the turbulent velocity field. The present approach proposes to compute the acoustic source terms directly from an unsteady field synthetized from the stochastic turbulence generation process proposed by Lafitte *et al.*[4] This stochastic method is based on the sweeping effect - or the fact that small scale structures are advected by the energy containing eddies - since this phenomenon is known to be a fundamental decorrelation mechanism of the velocity field.[10–13] For convenience, all the velocity fields introduced in this section will be written without the prime $< . >'$ even if it refer to fluctuating variables.

A. Overview of the model

The stochastic method[4,14] used in the framework of this study allows the generation of stochastic turbulent velocity fields. The synthetization process of these unsteady fields is based on the sweeping hypothesis. A separation in the turbulence scales is thus required. Following the former idea of Fung *et al.*,[12] the turbulent velocity field $\mathbf{u}$ is splitted into two parts respectively linked to the large and small scale structures:

$$\mathbf{u}(\mathbf{x},t) = \mathbf{u}_l(\mathbf{x},t) + \mathbf{u}_s(\mathbf{x},t) \tag{10}$$

The field $\mathbf{u}_l$ is provided by the Bailly and Juvé[15] method deriving straightforwardly from the former model of Kraichnan[16] while the field $\mathbf{u}_s$ is obtained from an adaptation of the Billson *et al.*[1] approach. The starting point to compute $\mathbf{u}_l$ and $\mathbf{u}_s$ is the local definition of an energy spectrum. Following the homogeneous isotropic turbulence hypothesis, a Von Kármán-Pao spectrum is imposed at each grid point depending on the local transport variables k_t and ε:

$$E(k) = \alpha_E \left(\varepsilon L_e\right)^{2/3} \left(kL_e\right)^{-5/3} f_L\left(kL_e\right) f_\eta\left(kL_\eta\right) L_e \tag{11}$$

where L_e, corresponding approximately to the length scale to whom the maximum of energy occurs,[17] is related to the local integral length scale L by the relation $L_e = L/0.747$; L being defined by:

$$L = \alpha_L (2/3k_t)^{3/2} \varepsilon^{-1} \tag{12}$$

and $L_\eta = (\nu^3/\varepsilon)^{1/4}$ designates the Kolmogorov length scale linked to the smallest turbulent motions in the flow. The choice of the calibration factor α_L in Eq. (12) has always been a topic of discussion and noticeably in the field of aeroacoustics, where this coefficient is determined by calibrating the model directly on the far-field acoustic spectra. However, Lafitte *et al.*[4] showed that, for a subsonic jet configuration with Mach number between 0.6 and 0.9, the approriate value for α_L is 1. This value is kept for the present study. In eq. (11), f_L and f_η are specified non-dimensional functions. The function f_L drives the shape of the energy-containing part of the spectrum while f_η represents its dissipation range. The specifications of f_L and f_η are:

$$\begin{cases} f_L\left(kL_e\right) = \left(\dfrac{kL_e}{\sqrt{1 + \left(kL_e\right)^2}} \right)^{17/3} \\ \\ f_\eta\left(kL_\eta\right) = \exp\left[-2\left(kL_\eta\right)^2 \right] \end{cases} \tag{13}$$

The function f_L defined in the relation (13) tends to unity for $kL_e >> 1$ and varies proportionally to $\left(kL_e\right)^4$ when $kL_e << 1$. Conversely, the definition of f_η in the relation (13) leads to $f_\eta \to 0$ for $kL_\eta << 1$. In the inertial subrange, the Kolmogorov -5/3 spectrum is recovered. In Eq. (11), the constant α_E is set to the value $1.2/\alpha_L^{-2/3}$. The Von Kármán-Pao energy spectrum is plotted in Fig. 6 for a given doublet (k_t, ε).

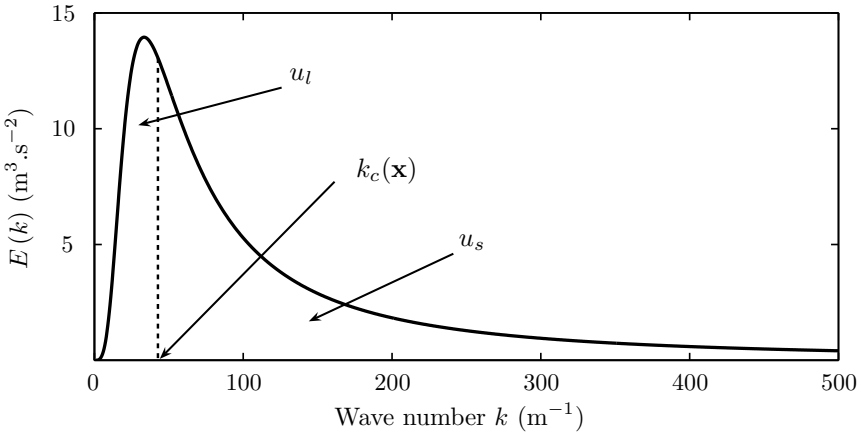

Figure 6. Contribution of $\mathbf{u}_l$ and $\mathbf{u}_s$ in a generic Von Kármán-Pao spectrum.

As shown in Fig. 6, the separation between large and small scales is achieved by introducing a cut-off wave number k_c. Since the sweeping hypothesis corresponds to the advection of the inertial range turbulent structures by the energy containing eddies,[18] k_c is chosen locally to fall just after the spectrum maximum:

$$k_c = 1.8 k_e = \frac{1.8}{L_e} \tag{14}$$

The energy spectrum is discretized using N modes of wave number k_n linearly distributed between a minimum wave number k_{min} and a maximum wave number k_{max}. One can remark that logarithmic distributions providing a better discretization of the spectrum E in the lower wave number range have been tested as well in Refs. 15, 19 but numerical results showed no major differences. In the case of inhomogeneous flowfield, k_c varies spatially so that the numbers of modes respectively linked to the large scale structures N_l and small scale structures $N_s = N - N_l$ vary spatially as well. However, the same wavenumber range $[k_{min}, k_{max}]$ is used for the whole computational domain.

1. Computation of the large scale velocity field $\mathbf{u}_l$

Following the expression proposed by Bailly and Juvé,[15] the velocity field $\mathbf{u}_l$ associated to the large scale eddies is decomposed as a sum of N_l Fourier modes:

$$\mathbf{u}_l(\mathbf{x},t) = 2\sum_{n=1}^{N_l} \mathrm{A_n}\cos\left(\mathbf{k_n}\left(\mathbf{x}-\mathbf{u_c}t\right)+\omega_\mathrm{n}t+\varphi_\mathrm{n}\right)\boldsymbol{\sigma}_\mathrm{n} \tag{15}$$

with amplitude $A_n = \sqrt{E(k_n)\Delta k_n}$ built from the Von Kármaán-Pao energy spectrum. $\mathbf{k}_n$ and φ_n are respectively the wave vector and the phase of the n^{th} mode. The isotropic nature of the modeled turbulence requires to pick $\mathbf{k}_n$ randomly on a sphere of radius $\|\mathbf{k}_n\| = k_n$. The incompressibility hypothesis imposes $\mathbf{k}_n \cdot \boldsymbol{\sigma}_n = 0$; the direction of the n^{th} mode $\boldsymbol{\sigma}_n$ is therefore perpendicular to $\mathbf{k}_n$. Further explanations concerning the parametrization of these parameters are given in the litterature.[19,20] In Eq. (15), the convection velocity $\mathbf{u}_c$ and the pulsation ω_n need imperatively to be constants of space in order to avoid a decorrelation of the generated velocity field at large times.[21] $\mathbf{u}_l$ being defined locally, $\mathbf{u}_c$ allows the modeling of the turbulent structures displacement in the downstream direction. For instance, for subsonic jet application, $\mathbf{u}_c$ might be set to $0.6\mathbf{u}_j$ in accordance with experiments,[22] where $\mathbf{u}_j$ designates the jet exit velocity. ω_n stands for the temporal pulsation of the n^{th} mode. The Kolmogorov pulsation defined by equation (16) is chosen for ω_n since it is the most appropriate choice for low wave numbers[23] and it gives more accurate results than, for instance, the Heisenberg pulsation.[17,24] To avoid spatial variations of ω_n, a mean value of the dissipation rate $<\varepsilon>$ is used to calculate ω_n where $<.>$ designates the average over the most energetic points, i.e all the points where k_t is greater than a prescribed threshold value $k_{threshold}$:

$$\omega_n = C_\mathrm{k}^{1/2} <\varepsilon>^{1/3} k_\mathrm{n}^{2/3} \tag{16}$$

The term $\mathbf{u}_l$ can therefore be explicitely formed at each time step of the numerical simulation. One can note that, by construction, $\mathbf{u}_l$ preserves the turbulent kinetic energy locally imposed to the large scale structures:

$$\frac{1}{2}\overline{u_{l_i}u_{l_i}} = \sum_{n=1}^{N_l} A_n^2 = \sum_{n=1}^{N_l} E(k)\Delta k \approx \int_{k_{min}}^{k_c} E(k)dk \tag{17}$$

2. Computation of the small scale velocity field $\mathbf{u}_s$

Fung *et al.*[12] wrote the temporal evolution of the small scale structures velocity field $\mathbf{u}_s$ as resulting from the association of advection and decorrelation processes. They wrote for a medium at rest:

$$\frac{\partial \mathbf{u}_s}{\partial t} = -\underbrace{\mathbf{u}_l\cdot\nabla\mathbf{u}_s}_{\text{advection}} - \underbrace{[(\mathbf{u}_s\cdot\nabla)\mathbf{u}_l + (\mathbf{u}_l\cdot\nabla)\mathbf{u}_s + 1/\rho\nabla p]}_{\text{decorrelation}} \tag{18}$$

In Eq. (18), p can not be explicitely modeled so that Fung *et al.* neglected the decorrelation term. In the present work, the building of the velocity field $\mathbf{u}_s$ linked to the small scale vortices can also be seen as an association of advection and decorrelation processes. $\mathbf{u}_s$, computed using a modified Billson *et al.* approach,[1] is defined by the following temporal filter:

$$\mathbf{u_s}(\mathbf{x},t) = a(\mathbf{x})\,\mathbf{v}(\mathbf{x},t) + b(\mathbf{x})\,\boldsymbol{\zeta}(\mathbf{x},t) \tag{19}$$

where $\mathbf{u}_s$ is written as a sum of an "advection term" $a(\mathbf{x})\,\mathbf{v}(\mathbf{x},t)$ and a "random term" $b(\mathbf{x})\,\boldsymbol{\zeta}(\mathbf{x},t)$ holding the decorrelation process. Unlike the works of Billson *et al.*[1,25] who resolve an advection equation with the conservative variables for $\mathbf{v}$, the advected term is here considered to be the small scale velocity field at the previous time step advected by the vector field $(\mathbf{u}_{bulk}+\mathbf{u}_l)$, $\mathbf{u}_{bulk}$ being a carrier velocity vector field. In other words, $\mathbf{v}$ is obtained by solving the advection equation (20) that ensures the modeling of the sweeping effect:

$$\frac{\partial \mathbf{u}_s^{t-\Delta t}}{\partial t} + \left(\mathbf{u}_{bulk}+\mathbf{u}_l^{t-\Delta t}\right)\cdot\nabla\mathbf{u}_s^{t-\Delta t} = \mathbf{0} \tag{20}$$

One can note that, in the Fung *et al.*[12] study, $\mathbf{u}_s$ was simply advected by the field $\mathbf{u}_l$ because of a zero mean velocity field. In Eq. (19), the "random term" $\boldsymbol{\zeta}$ is a sum of N_s spatial Fourier modes:

$$\boldsymbol{\zeta}(\mathbf{x}) = 2 \sum_{n=N_l+1}^{N} \mathrm{A_n} \cos\left(\mathbf{k_n} \cdot \mathbf{x} + \varphi_n\right) \boldsymbol{\sigma}_\mathrm{n} \tag{21}$$

where the set up of the stochastic parameters A_n, $\mathbf{k}_n$, φ_n and $\boldsymbol{\sigma}_n$ is achieved the same way than for $\mathbf{u}_l$ except that they are regenerated at each iteration. Consequently, $\boldsymbol{\zeta}$ is a temporal suite of uncorrelated field constituting a locally white noise with zero statistical mean value in time. This term therefore ensures the progressive decorrelation of $\mathbf{u}_s$. In Eq. (19), the definition of $a = e^{-t/\tau_c}$ guarantees the exponential decorrelation of the velocity field according to a caracteristic time scale $\tau_c = k_t/\varepsilon$. $b = \sqrt{1-a^2}$ allows the conservation of the turbulent kinetic energy in k_t homogeneous flows.

B. Description of the algorithm numerical implementation

The initialization of the computation is achieved by calculating $\mathbf{u}_l(x, t_0)$ and imposing $\mathbf{u}_s(x, t_0) = \boldsymbol{\zeta}(x, t_0)$. For a detailed explanation of the manner the algorithm works, one resumes the different steps of the method. At each iteration,

- The field $\mathbf{u}_l$ is the first to be generated from eq. (15).
- Once done, the velocity field $\mathbf{u}_s^{t-\Delta t}$ linked to the small scale structures at the previous time step is advected by the vector field $(\mathbf{u}_{bulk} + \mathbf{u}_l^{t-\Delta t})$ to obtain $\mathbf{v}$ from eq. (20).
- The white noise $\boldsymbol{\zeta}$ is generated from eq. (21).
- The term $\mathbf{u}_s$ is computed and finally, the turbulent velocity field $\mathbf{u}$ is formed using eq. (10).
- $\mathbf{u}_l$ and $\mathbf{u}_s$ are then stored in order to solve the advection equation (20) at the next time step.

C. Caracteristics of the sweeping based turbulence generation process

The synthetized turbulent velocity fields generated by this stochastic model are proven to respect some aerodynamic statistical features of the flow such as two-points two-times velocity correlation functions. The spatial distribution of the most energetic points in the turbulent kinetic energy mapping reconstructed from the generated field is also preserved assuming a slight of energy due to the medium inhomogeneity.[4] It includes the shear effects on the turbulence due to the presence of an inhomogeneous mean flow and it deals correctly with the convection velocity of the eddies in the shear layer. For further details, the validation study of the present method is presented in Refs. [4, 14].

IV. Application to a subsonic jet configuration

The validated numerical tool constituted of the coupling between the sweeping based turbulence generation process presented in section III and the Euler solver introduced in section II is applied to a free subsonic jet - the jet Φ_{80} - since the confined geometry is too complicated to be studied at first. The Mach number of the configuration is M=0.72 and the diameter of the nozzle is $D = 80$ mm. A RANS computation of the subsonic jet Φ_{80}, validated in Ref. [4], has therefore been used to access the mean flow and transport variables needed to synthetize the stochastic turbulence and to represent the averaged mean flow in the linearized Euler equations.

A. Computational set up

The cartesian grid used in the present work, consisting of $361 \times 284 \times 184$ mesh points, extends up to $30D$ in the flow direction and is bounded by $[-4D, 17D]$ in the $y-$direction and $[-4D, 4D]$ in the $z-$direction. The spatial resolution in the vicinity of the nozzle exit is defined by $\Delta x = 5$ mm and $\Delta y = \Delta z = 2.5$ mm. This resolution, held up to 20 diameter in the $x-$direction, is able to support an acoustic wave number $k_{max} = 200$ m^{-1} which is a good compromise between the modeling of the aerodynamic quantities and the computation cost. The finest resolution is held up to $2.5D$ from the jet axis in the $y-$ and the $z-$direction. A damping zone is set up from $x = 16D$ to the exit of the domain to avoid spurious reflections that could contaminate the final solution. A stretching of the mesh in the downstream direction is applied in this region

in order to improve efficiency of the artificial numerical dissipation. 100 modes are used to discretize the Von Kármán-Pao spectra. These modes are linearly distributed in the interval $2 \leq k_n \leq k_{max} = 200$ m^{-1}. The stochastic velocity field is generated at each grid point of the computational domain but the source vector, defined with $\beta = 1$, is only injected where $k_t \geq k_{\text{threshold}} = 900$ m^2.s^{-2}, corresponding to the half of the maximum turbulent kinetic energy in the domain. The time step Δt is set to 3.5×10^{-6}s based on a CFL number of 0.86. 30 000 temporal iterations are performed on 252 processors. Computation is achieved in approximately 30 hours on such a cluster. Furthermore, the computation could have been run on more processors, so that the retriaval time would be reduced.

B. Far-field acoustic spectra

The pressure signals in the far-field are directly obtained from *sAbrinA_v0*. Associated power spectral densities are computed using 0.98 s of physical time with a sampling frequency of $1/10\Delta t$ and plotted in Fig. 11 for 4 different observers located on an arc of radius $R = 10D$ from the nozzle exit. The observers are located respectively at 45^o, 60^o, 70^o and 80^o from the jet axis. Numerical results are compared to experimental data provided by the Onera.

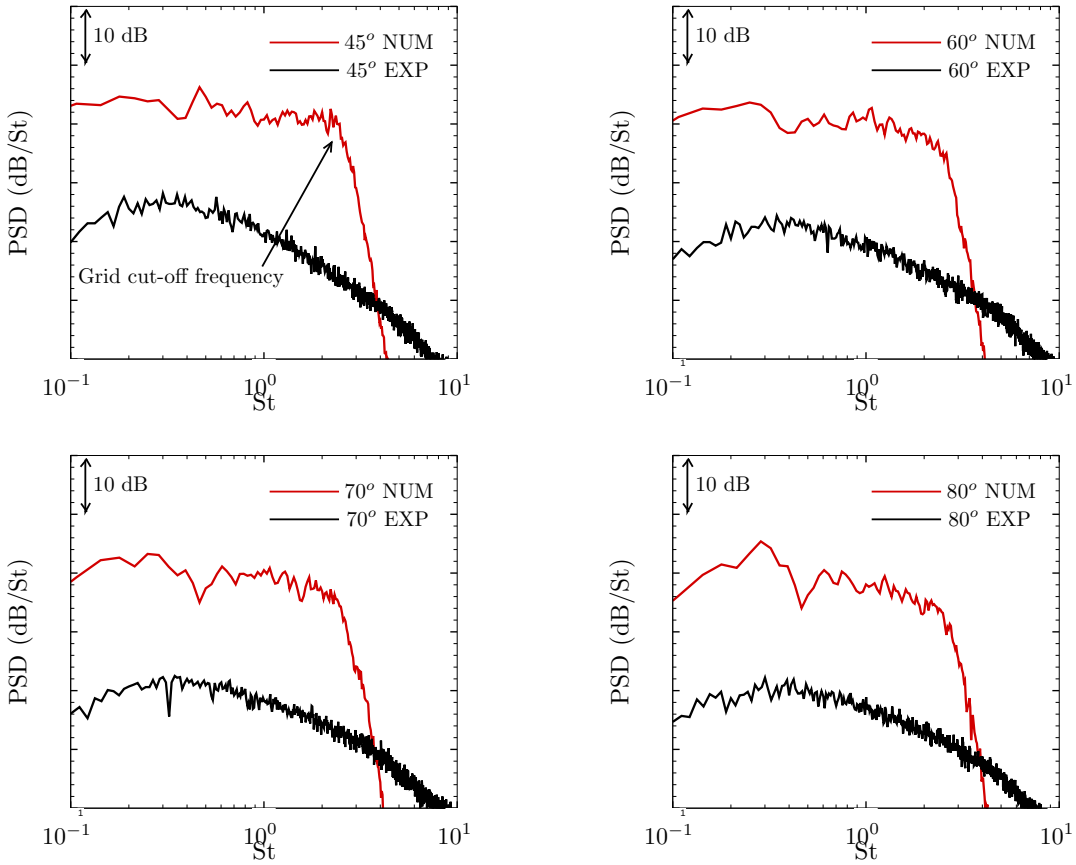

Figure 7. Power spectral density of the far-field pressure signals for observers located at $r = 10D$, $\theta = 45^o$, 60^o, 70^o and 80^o.

The power spectral densities of the far-field pressure signals show an amplitude shift of more than 10 dB . The amplitude of the pressure signals reveals to be overestimated by a factor 10 at all angles. This phenomenon, already observed in the literature,[1,26] confirms that methodologies relying on source terms computation from stochastic fields have a tendency to overestimate the noise radiated by flows. Commonly, this issue is solved by modifying the parametrization of the calibration factor α_L in Eq. (12). However, this is not the appropriate way to proceed since this modification directly impact the energy distribution among the turbulent modes and so the amount of energy injected in the calculation.[4] One can remark that the cut-off frequency shown by the spectra is consistent with the spatial resolution of the grid in the far-field.

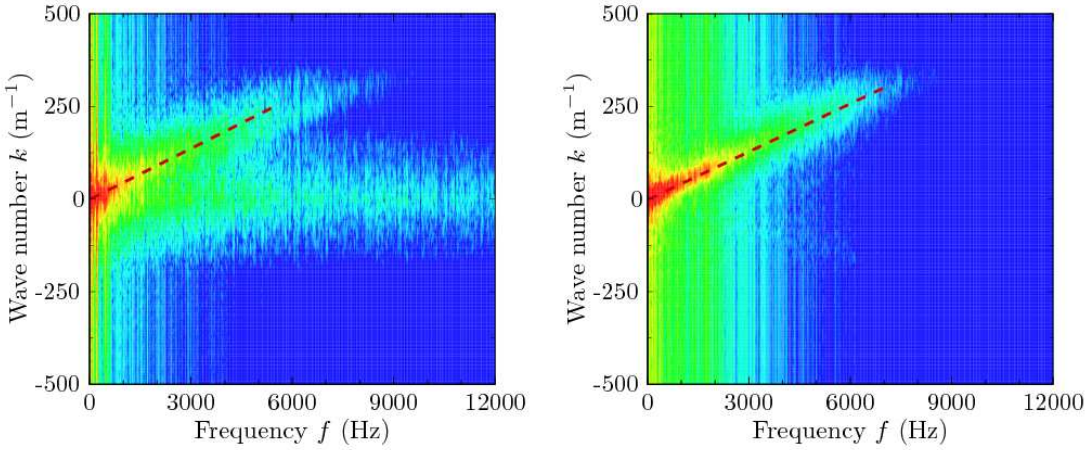

a)

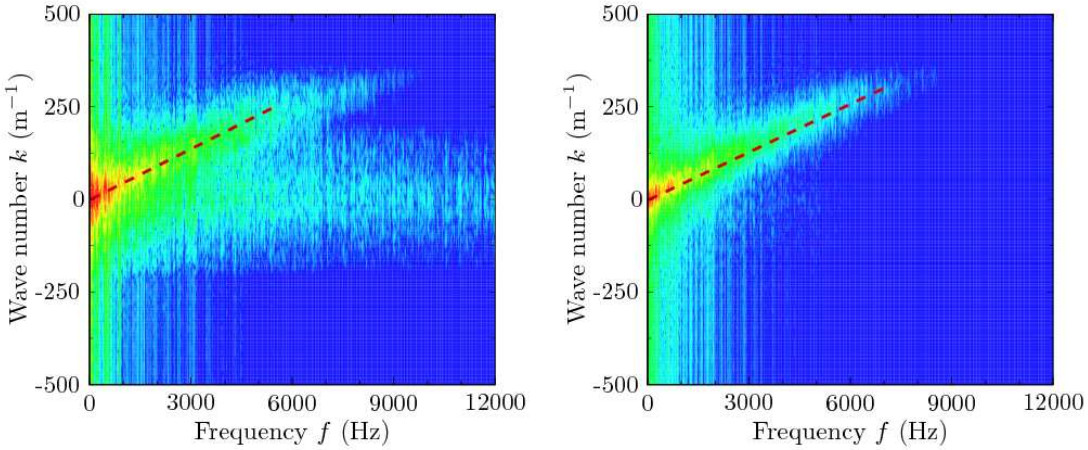

b)

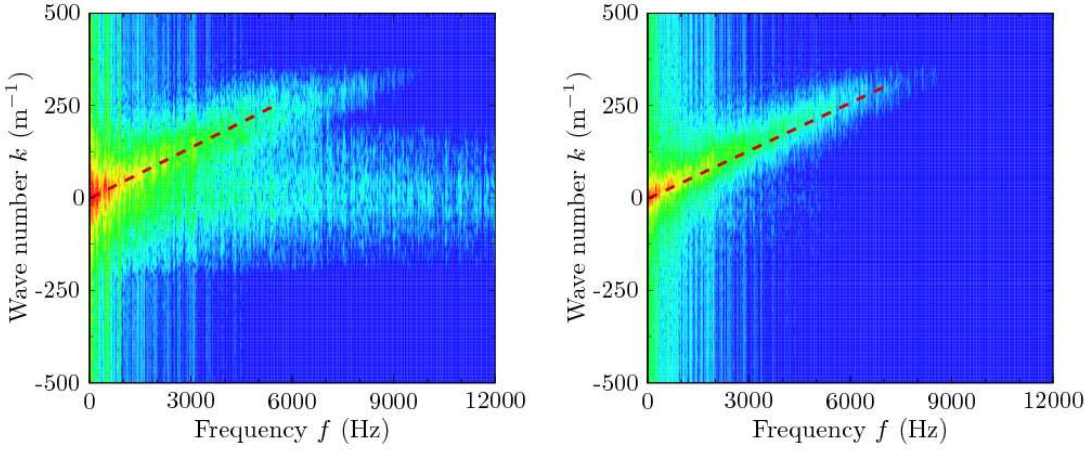

c)

Figure 8. $k-f$ **spectra based on the velocity components from the stochastic model (on the left) and the Euler equations (on the right). The reference point is** $(5D, 0.5D)$**.** *a*) u_1 **component,** *b*) u_2 **component,** *c*) u_3 **component. Levels are taken between 0 and 80 dB on the left against 0 and 100 dB on the right.**

C. Analysis of the Euler perturbed field

The stochastic method is proven to deal correctly with the effects of the mean flow on turbulence and the convection of the turbulent structures. The approach noticeably allows the reproduction of the two-points two-times velocity correlation functions while it preserves the spatial distribution of the turbulent kinetic energy k_t assuming a slight loss of energy. Nevertheless, the response of the Euler perturbed velocity field to the forcing of the LEE by source terms computed directly from this stochastic field has to be studied to understand the amplitude problem occuring in the far-field acoustic spectra.

First, the way the perturbed velocity field assimilates the convection effects imposed by the stochastic field is investigated by computing wave number-frequency spectra $k-f$ in the shear layer using a longitudinal rake of probes. The reference point is $(5D, 0.5D)$ and the rake is constitued of 117 points. $\Delta x = 5$ mm so that the rake extends up to $7.25D$ downstream of the reference point. 1 average and a Hanning windowing are applied on the time signals using a sampling frequency $f_e = 1/10\Delta t$ so that the physical time used to compute the spectra is $750T_e$. This configuration leads to a wave number resolution of $\Delta k = 5$ m^{-1}, a frequency step of $\Delta f = 19$ Hz and an error due to the resolution of 2.3%. The $k-f$ spectra, obtained from the three components of the stochastic velocity field and plotted on the left in Fig. (8), present two different slopes. The first gives access to the convection velocity of the turbulent structures: $u_c = 0.55u_j$. Assuming that Fleury *et al.*[22] showed that the mean convection velocity of the turbulent structures in the shear layer is approximately $u_c = 0.6u_j$, the error of the approximation is about 9%. The presence of the other slope, corresponding to an infinite velocity of propagation, is due to the fact that the $k-f$ spectra have been computed using only a one-dimensional rake. Evaluating the convection velocity u_c from the perturbed velocity field spectra plotted on the right of Fig. (8), one find $u_c = 0.58u_j$, corresponding to an error of about 5% in comparison with Fleury *et al.* results.[22]

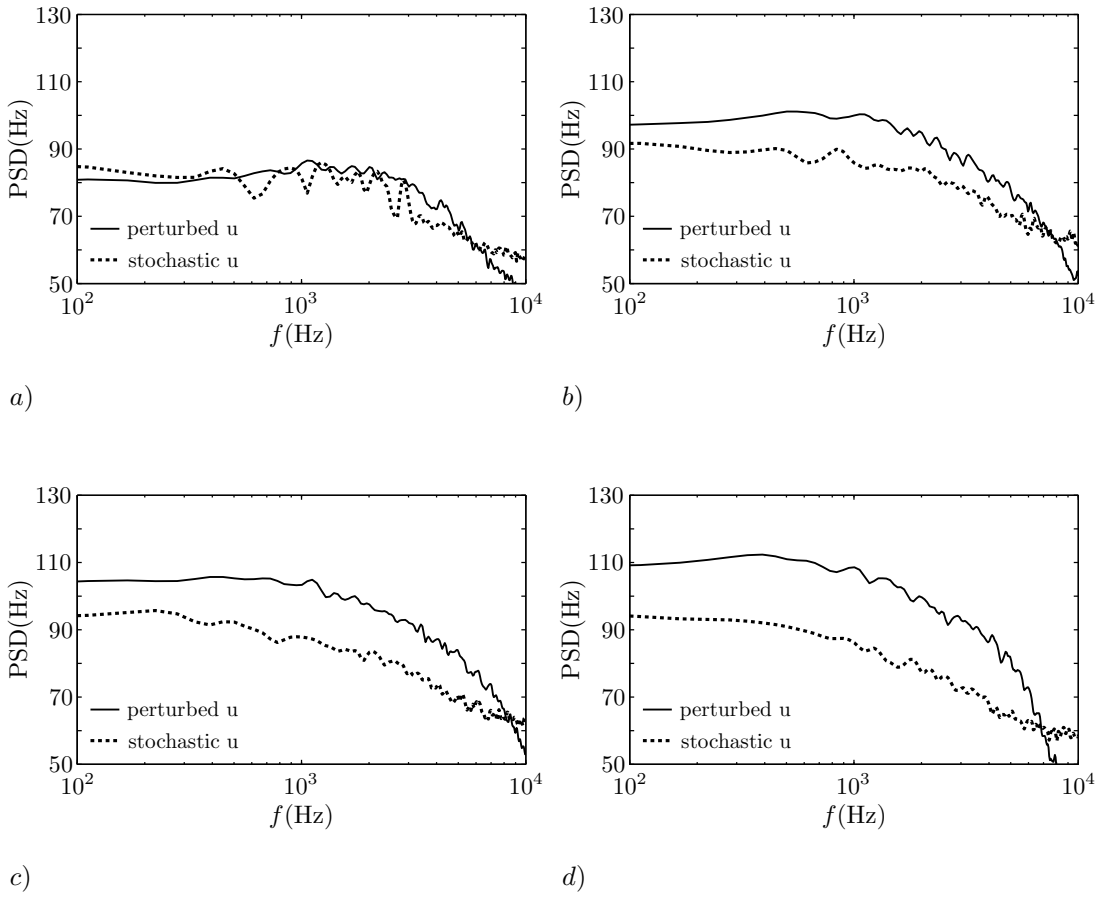

Figure 9. Power spectral density of the longitudinal component of the velocity u_1 along the axis $y = 0.5D$. *a)* $x = 1.5D$, *b)* $x = 4D$, *c)* $x = 6.5D$, *d)* $x = 11.5D$

In a second time, probes located at the center of the shear layer, on the axis $y = 0.5D$, have been extracted from the simulation and power spectral densities of the three velocity components have been performed to compare the spectral contents of the stochastic and the perturbed velocity fields. Power spectral densities of the longitudinal component u_1 of the turbulent velocity field are plotted in Fig. 9 for four probes located respectively at $x = 1.5D$, $x = 4D$, $x = 6.5D$ and $x = 11.5D$ from the nozzle exit. In the vicinity of the nozzle exit, the power spectral density levels are low because of the weak amount of injected energy due to the spatial resolution of the grid that does not allow a sufficient discretization of the Von Kármán-Pao spectra. In one hand, the PSD levels of the stochastic velocity u_1 increase from $x = 1.5D$ to $x = 6.5D$ and stabilizes between $x = 6.5D$ and $x = 11.5D$. On the other hand, the PSD levels of the perturbed field increase consistently from $x = 1.5D$ to $x = 11.5D$. The shift of amplitude between the PSD of the stochastic and the perturbed fields therefore increases with the longitudinal position x. This shift of amplitude, nearly equal to 0 in the vicinity of the nozzle exit, reaches 15 dB at $x = 11.5D$. Despite this phenomenon, one can remark that the spectral content of the perturbed velocity field at each position is comparable to those of the stochastic velocity field.
Fig. (10) depicts the instantaneous source term injected in the u_1-momentum equation at the time $t = 900\Delta t$, superimposed to the turbulent kinetic energy isocontours provided by the RANS computation. The most energetic sources are located in the energetic lobes caracterizing the subsonic jet. The acoustic sources that contribute to the acoustic radiation are mostly located between $x = 0$ and $x = 11D$. The turbulent kinetic energy reconstructed from the Euler perturbed velocity field has been computed during the calculation and compared to the energy provided by the steady RANS computation. By averaging on all the grid points of non-zero energy and of longitudinal position $x < 11D$, the ratio between these two quantities is nearly equal to 9.3; which is consistent with the amplitude shift occuring for the far-field acoustic spectra, the pressure signals being surestimated by a factor 10.

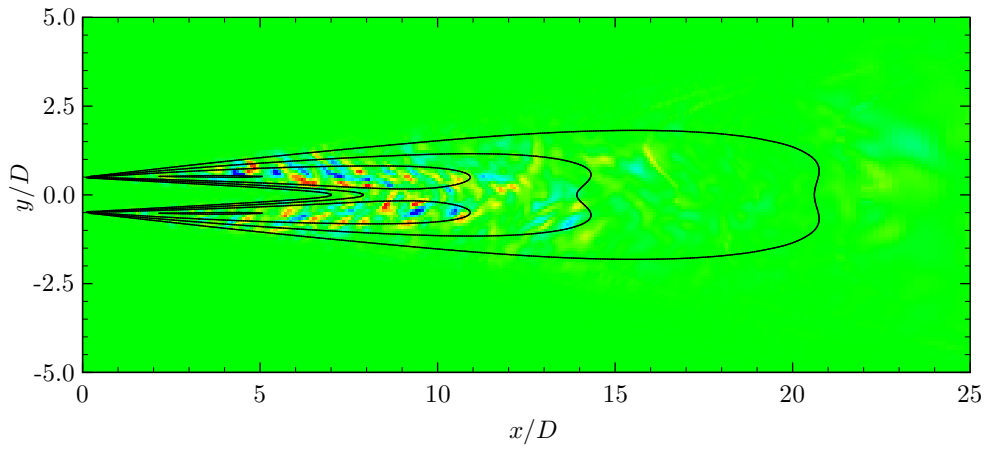

Figure 10. Source term of the momentum equation along the $x-$direction $\frac{\partial}{\partial x_j}\overline{\rho}u_1u_j$. The levels are included between -0.00025 and 0.00025 kg.m^{-2}.s^{-2}. ▬ Isocontours of the turbulent kinetic energy k_t provided by the RANS computation. Levels are from 450 to 1800 m^2.s^{-2} with a step of 450 m^2.s^{-2}.

D. Corrected far-field acoustics spectra

The simulation presented in section IV.A is performed a second time by changing the value of the factor β to 1/10 accordingly to the shift of amplitude observed for the perturbed pressure and energy. Power spectral densities of the pressure signals at the four observers located at $\theta = 45^o$, 60^o, 70^o and 80^o on an arc of radius $R = 10D$ from the nozzle exit are plotted in Fig. 11 and compared to experimental data provided by the Onera. One can notice that the amplitude of the power spectral densities are correctly mimicked for all the observers. At small angles, i.e at $\theta = 45^o$, the power spectral density of the simulation is almost flat so that

experimental spectrum is not reproduced. Nevertheless, as θ increases, the numerical plots get closer to the experimental curves so that, for the observers at $\theta = 70^o$ or 80^o, the central frequency of the spectrum is correctly mimicked. One can notice that for those observers, the slope of the spectra at high frequencies, i.e after the spectrum maximum, is in good agreement with the experimental one.

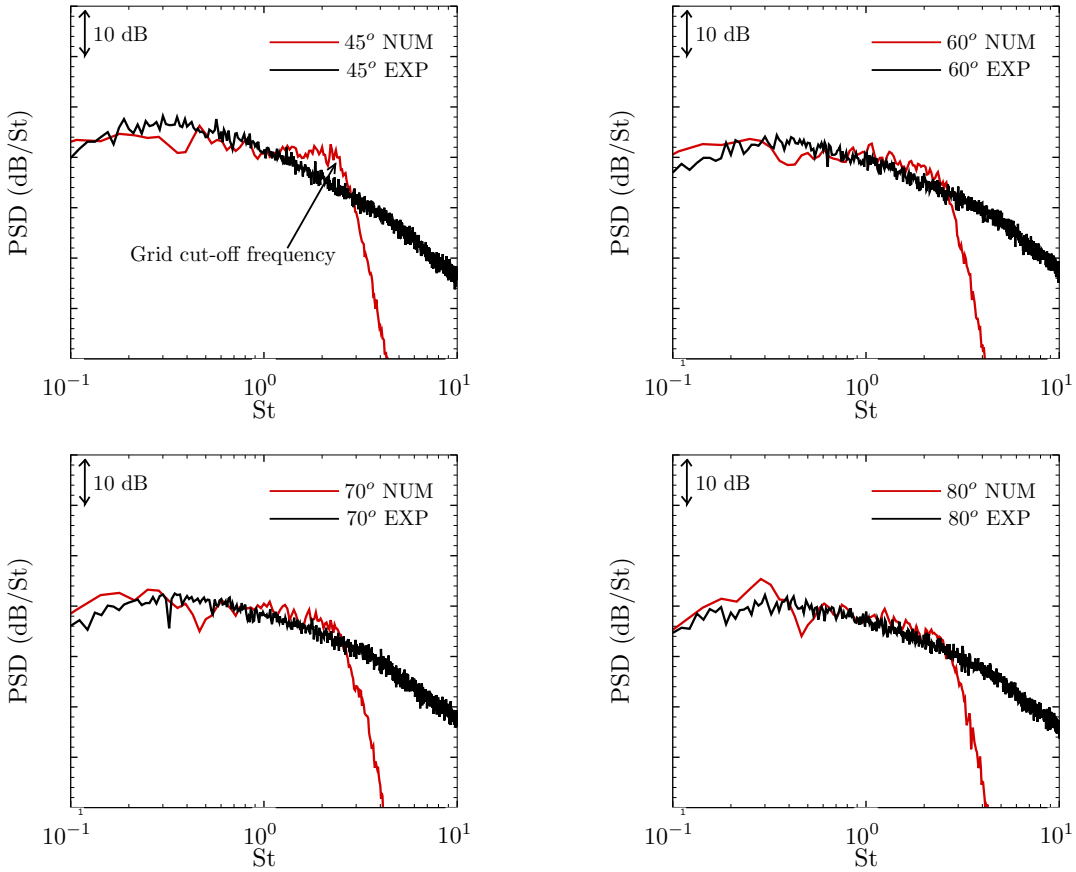

Figure 11. Power spectral density of the far-field pressure signals for observers located at $r = 10D$, $\theta = 45^o$, 60^o, 70^o and 80^o obtained with the calibrated source terms.

V. Conclusion

A predictive tool for far-field acoustics, consisting of the coupling between the sweeping based turbulence generation process[4,14] and Onera's *sAbrinA_v0* Euler solver, has been introduced in this paper. The idea is to compute acoustic source terms from a stochastic velocity field and to inject it directly in the linearized Euler equations through a non-linear source term. This numerical solver is noticeably able to preserve the multipolar features of a given source and to reproduce the acoustic refraction effects due to the wave propagation through sheared mean flow, as shown by the test cases performed in section II.C. The resulting numerical tool has been validated by studying a cold free jet at M= 0.72. First investigations showed that the forcing of the Euler perturbed fields by the stochastic source terms lead to an overestimation of the amplitude of the far-field acoustic spectra, despite a satisfying modeling of its spectral content. An analysis of the enforced Euler velocity field revealed that an amplification phenomenon impacting the perturbed velocity field - and consequently the turbulent kinetic energy that this velocity field is holding - occurs during the computation. Simulations has therefore been performed with a source vector calibrated by a factor β corresponding to the ratio between the overestimated energy reconstructed from the Euler velocity field and the turbulent kinetic energy provided by the steady RANS calculation. Final results show that acoustic spectra are well modeled for large angles in terms of amplitude, central frequency and slope at high frequencies. Nevertheless, a problem still occurs for small angles. The next step of this study is to apply the numerical tool presented in the present work to the confined jet geometry configuration. Numerical results

will be compared to aerodynamic and acoustic data obtained during a measurement campaign led at the Ecole Centrale de Lyon.

Acknowledgement

This study has been conducted in the framework of a Ph.D Thesis founded by Liebherr Aerospace Toulouse and conducted in the Computational Fluid Dynamics and Aeroacoustics Department of the Onera in association with the Ecole Centrale Lyon.

References

[1]Billson, M., Eriksson, L., and Davidson, L., "Jet noise prediction using stochastic turbulence modeling," *9th AIAA/CEAS Aeroacoustics Conference, AIAA Paper 2003-3282*, Hilton Head, South Carolina, 12-14 May 2003.

[2]Ewert, R., "Broadband slat noise prediction based on CAA and stochastic sound sources from a fast Random Particle-Mesh (RPM) method," *Computers and Fluids*, Vol. 37, 2008, pp. 369–387.

[3]Bailly, C. and Juv, D., "Numerical solution of acoustic propagation problems using linearized Euler equations," *AIAA Journal*, Vol. 38, No. 1, 2000, pp. 22–29.

[4]Lafitte, A., Laurendeau, E., Le Garrec, T., and Bailly, C., "A study based on the sweeping hypothesis to generate stochastic turbulence," *17th AIAA/CEAS Aeroacoustics conference*, Portland, Oregon, 5-8 June 2011.

[5]Redonnet, S., Manoha, E., and Sagaut, P., "Numerical simulation of propagation of small perturbations interacting with flows and solid bodies," *7th AIAA/CEAS Aeroacoustics conference*, Maastricht, Netherlands, May 2001.

[6]Redonnet, S., *Simulation de la propagation acoustique en présence d'écoulements quelconques et de structures solides, par résolution numérique des équations d'Euler*, Ph.D. thesis, Universit Bordeaux I, 2001.

[7]Guenanff, R., *Couplage instationnaire Navier-Stokes/Euler pour la génération et le rayonnement des sources de bruit aérodynamique*, Ph.D. thesis, Universit de Rennes, 2004.

[8]Bogey, C., Bailly, C., and Juvé, D., "Computation of flow noise using source terms in linearized Euler's equations," *AIAAJ*, Vol. 40, No. 2, 2002, pp. 235–243.

[9]Grverie, L. and Bailly, C., "Construction d'un oprateur de propagation partir des équations d'Euler linéarisées," *C. R. Acad. Sci.*, Vol. 326, No. II b, 1998.

[10]Chen, S. and Kraichnan, R., "Sweeping decorrelation in isotropic turbulence," *PFA*, Vol. 1, 1989, pp. 2019–2025.

[11]Nelkin, M. and Tabor, M., "Time correlations and random sweeping in isotropic turbulence," *Phys. Fluids A*, Vol. 2, No. 1, 1990, pp. 81–83.

[12]Fung, J., Hunt, J., Malik, N., and Perkins, R., "Kinematic Simulation of Homogeneous Turbulence by Unsteady Random Fourier Modes," *J. Fluid Mech.*, Vol. 236, 1992, pp. 281–318.

[13]Praskovsky, A., Gledzer, E., Kuryakin, M., and Zhou, Y., "The sweeping decorrelation hypothesis and energy-inertial scale interaction in high Reynolds number flows," *J. Fluid Mech.*, Vol. 248, 1993, pp. 493–511.

[14]Lafitte, A., Laurendeau, E., Le Garrec, T., and Bailly, C., "Application of a sweeping based stochastic method to compute free jets acoustic sources," *Acoustics conference*, Nantes, France, 23-17 April 2012.

[15]Bailly, C. and Juvé, D., "A stochastic approach to compute subsonic noise using linearized Euler's equations," *5th AIAA/CEAS Aeroacoustics Conference, AIAA Paper 99-1872*, Seattle, Washington, 10-12 May 1999.

[16]Kraichnan, R., "Diffusion by a random velocity field," *Phys. Fluids*, Vol. 13, 1970, pp. 22–31.

[17]Bailly, C., Gloerfelt, X., and Bogey, C., "Report on stochastic noise source modelling," Tech. rep., Projet JEAN, 2002.

[18]Siefert, M. and Ewert, R., "Sweeping sound generation in jets realized with a random particle-mesh method," *15th AIAA/CEAS Aeroacoustics Conference, AIAA Paper 2009-3369*, Miami, Florida, 11-13 May 2009.

[19]Bechara, W., Bailly, C., Lafon, P., and Candel, S., "Stochastic approach to noise modeling for free turbulent flows," *AIAA Journal*, Vol. 32, No. 3, 1994, pp. 455–463.

[20]Omais, M., Caruelle, B., Redonnet, S., Manoha, E., and Sagaut, P., "Jet noise prediction using RANS CFD input," *5th AIAA/CEAS Aeroacoustics Conference, AIAA Paper 2008-2938*, Vancouver, Canada, 5-7 May 2008.

[21]Batten, P., Goldberg, U., and Chakravarthy, S., "Reconstructed sub-grid methods for acoustic predictions at all Reynolds numbers," *8th AIAA/CEAS Aeroacoustics Conference, AIAA Paper 2002-2511*, Breckenridge, Colorado, 17-19th June 2002.

[22]Fleury, V., Bailly, C., Jondeau, E., Michard, M., and Juvé, D., "Space-time correlations in two subsonic jets using dual particle image velocimetry measurements," *AIAA Journal*, Vol. 46, No. 10, 2008, pp. 2498–2509.

[23]Favier, B., Godeferd, F., and Cambon, C., "On space and time correlations of isotropic and rotating turbulence," *Phys. Fluids*, Vol. 22, 2010.

[24]Gloerfelt, X., Bailly, C., and Bogey, C., "Full 3-D application of the SNGR method to isothermal Mach 0.9 jet," Tech. rep., JEAN project, 2003.

[25]Billson, M., Eriksson, L., Davidson, L., and Jordan, P., "Modeling of synthetic anisotropic turbulence and its sound emission," *10th AIAA/CEAS Aeroacoustics Conference, AIAA Paper 2004-2858*, Manchester, England, 10-12 May 2004.

[26]Dembinska, F., *Modélisation stochastique des sources acoustiques générées par la turbulence : application au bruit de jet*, Ph.D. thesis, Universit Pierre et Marie Curie, 2009.